Memristive arrangements of nanofluidic pores

Patricio Ramirez [1,*] Sergio Portillo [2] Javier Cervera [2] Juan Bisquert [3] and Salvador Mafe [2,4]

[1]*Departament de Física Aplicada, Universitat Politècnica de València, E-46022 València, Spain*
[2]*Departament de Física de la Terra i Termodinàmica, Universitat de València, E-46100 Burjassot, Spain*
[3]*Institute of Advanced Materials (INAM), Universitat Jaume I, 12006 Castelló, Spain*
[4]*Allen Discovery Center at Tufts University, Medford, Massachusetts 02155, USA*

(Received 3 January 2024; accepted 29 March 2024; published 24 April 2024)

We demonstrate that nanofluidic diodes in multipore membranes show a memristive behavior that can be controlled not only by the amplitude and frequency of the external signal but also by series and parallel arrangements of the membranes. Each memristor consists of a polymeric membrane with conical nanopores that allow current rectification due to the electrical interaction between the ionic solution and the pore surface charges. This surface charge-regulated ionic transport shows a rich nonlinear physics, including memory and inductive effects, which are characterized here by the current-voltage curves and electrical impedance spectroscopy. Also, neuromorphiclike potentiation of the membrane conductance following voltage pulses (spikes) is observed. The multipore membrane with nanofluidic diodes shows physical concepts that should have application for information processing and signal conversion in iontronics hybrid devices.

DOI: 10.1103/PhysRevE.109.044803

I. INTRODUCTION

Micro and nanofluidic memristors are attracting wide interest for computation and signal processing [1–11]. We have described recently a multipore memristor with a broad range of tunable conduction properties [12]. Surface charge-regulated ionic transport through nanofluidic conical pores show current rectification phenomena due to the electrical interaction between the ionic solution and the pore surface charges [13–15]. Because of the analogies between liquid-state ionic memristors and biological ion channels [16–18], the fundamental concepts involved are also relevant to biophysics. Also, electrochemical circuits based on nanofluidic diodes operating in ionic solutions are central to sensors and actuators for information processing, controlled release, and signal conversion in biomedicine and biotechnology [2–5,10,18].

The physical functionality of single memristors can be expanded further by demonstrating the feasibility of operational arrangements in ionic circuits where the control of electrical signals can benefit from scalability and unit integration [2–4,10,18,19]. Here, we demonstrate that different series and parallel arrangements of multipore membranes with nanofluidic conical pores can show significant memory and memristive effects. Remarkably, neuromorphiclike potentiation of the membrane conductance caused by voltage pulses (spikes) can also be observed.

II. EXPERIMENT

The experimental system is shown in Fig. 1. The multipore membranes are obtained by irradiating 12.5-μm- thick polyimide (PI) foils with swift heavy ions at the linear accelerator UNILAC (GSI, Darmstadt). The conversion of the resulting ion tracks into approximately conical nanopores is realized by means of asymmetric track-etching techniques [20–22]. Scanning electron microscope imaging, together with pore electrical conductance measurements, suggest that the orders of magnitude of the cone radii are 10 nm for the tip and 100 nm for base [15]. At $p\mathrm{H} = 7$, the surface pore charges result from the ionization of the carboxylate residues, which gives typical charge densities between -0.1 and $-1.0\ e/\mathrm{nm}^2$, where e is the elementary charge, in 100-mM KCl [13–15]. In general, however, the pH dependence of the surface pore charge leads to a quasineutral pore at pH values between 3 and 4 and to a positively charged pore at $p\mathrm{H} = 2.0$ [12,15]. Thus, the rectification and memory effects can be modulated by changing the pH of the aqueous solutions. The exposed membrane area ($1\ \mathrm{cm}^2$) is placed between two ionic solutions where Ag|AgCl electrodes with 2-M KCl solution salt bridges are immersed to control voltage (V) and current (I) with a BioLogic SP-200 potentiostat (Fig. 1). Good reproducibility of the membrane rectification properties due to the spatially inhomogeneous charge distribution along the conical axis is found, as shown previously [13–15].

III. RESULTS AND DISCUSSION

Figures 2(a) and 2(b) show the $I-V$ curves of membrane samples 1 and 2 with approximately 300 pores. The steady state curves are measured with a triangular potential wave at the scanning rate 200 mV/s, equivalent to an external voltage signal of frequency $f = 25$ mHz for a voltage amplitude of $V_0 = 2$ V. They show no hysteresis because the period of this signal is higher than the characteristic time needed for the redistribution of the mobile ions in the charged pore solution [12]. The conical pores show a high resistance when the current enters the cone base and a low resistance when

*patraho@fis.upv.es

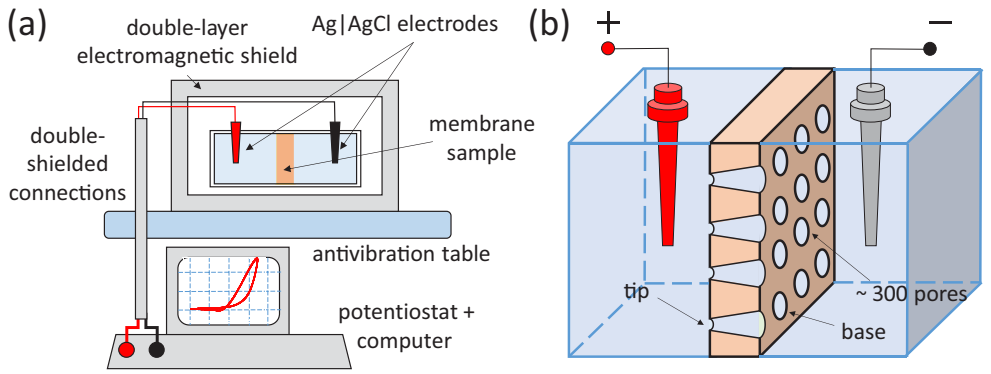

FIG. 1. (a) In the experimental setup, the electrochemical cell connected to the potentiostat is placed within a magnetic shield mounted on an antivibration table. (b) Schematic of the cell with the multipore membrane and the Ag|AgCl electrodes.

the current enters the cone tip [13]. Note the similar $I-V$ characteristics of the two samples. The data show a transition from capacitive hysteresis in the negative voltage domain, to inductive hysteresis in the positive voltage domain, according to the general theory of hysteresis [23].

The hysteretic curves of Figs. 2(a) and 2(b) are obtained with a sinusoidal wave of frequency $f = 20$ Hz. The high membrane conductance observed at voltages $V > 0$ is due to the accumulation of mobile cations at the cone tip. Thus, hysteretic effects occur if the ionic solution at the cone tip cannot follow instantaneously the changes of the driving signal, so that the membrane behaves as a chemical inductor because of the resulting memory effects. As expected, the hysteresis effects are much higher for $V > 0$ (ion accumulation) than for $V < 0$ (ion depletion). For high frequencies (100 Hz), memory and rectification effects decrease [12]. These experimental facts are characteristic of memristors [24,25] and show also reminiscences to biomimetic nanopores and biological channels [1,3,16,18]. No evidence of electrolysis phenomena was observed in the solutions and currents.

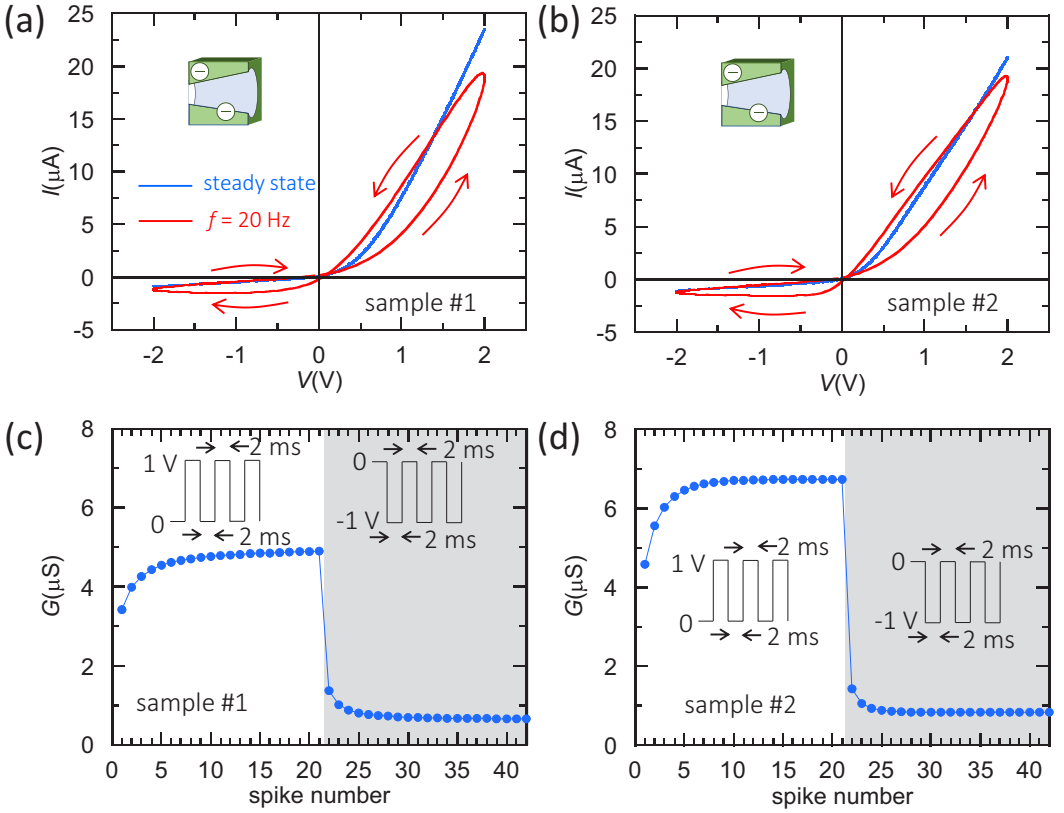

FIG. 2. (a) Current (I)–voltage (V) curves for membrane sample 1 measured with a sinusoidal wave at the voltage amplitude $V_0 = 2$ V and the frequency $f = 20$ Hz in a 0.1-M KCl solution (*red* lines). The steady-state curve (blue line) obtained at low signal frequency (25 mHz) is also shown. The arrows indicate the time evolution of the output current and the inset shows the pore arrangements. (b) $I-V$ curve for sample 2. (c) Conductance (G) vs spike number curves showing the membrane sample 1 response to a sequence of individual 2-ms positive and negative voltage pulses (spikes) of amplitude $V_p = 1$ V (insets). (d) G vs spike number curves for sample 2.

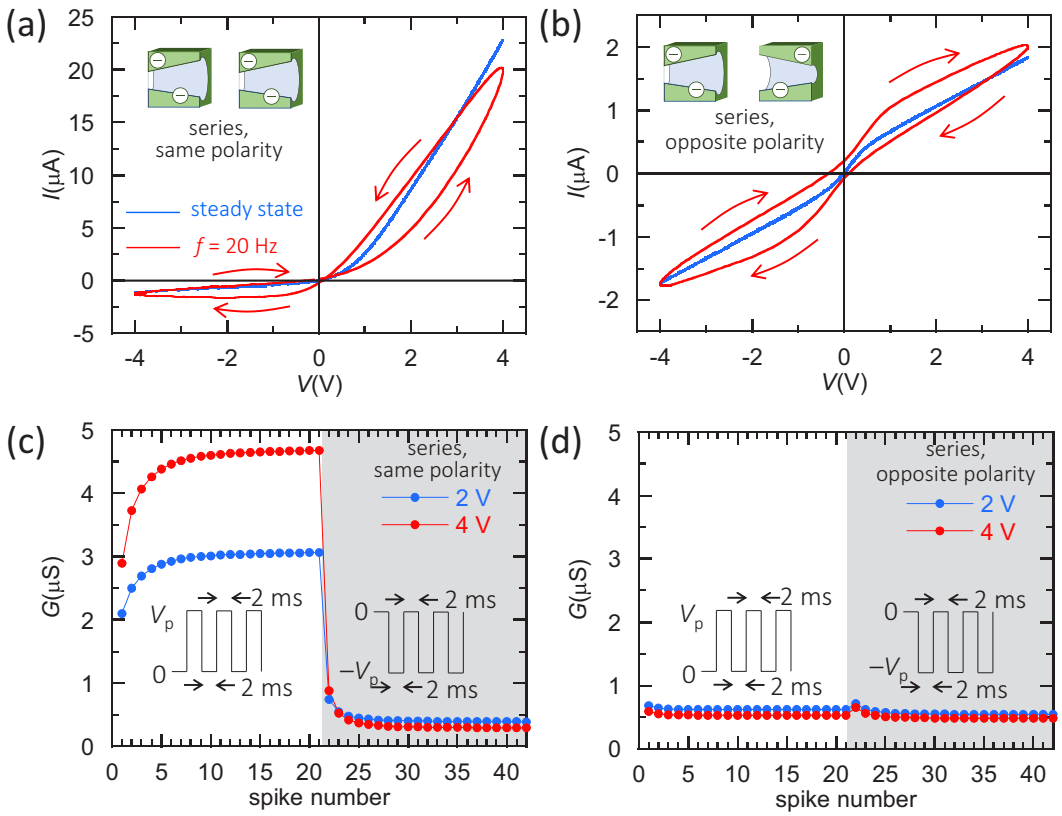

FIG. 3. (a) $I-V$ curve for samples 1 and 2 at $V_0 = 4$ V and $f = 20$ Hz in a 0.1-M KCl solution (red lines) for the series arrangement with the pores in the same polarity (inset). The steady-state curve (blue line) obtained at low signal frequency is also shown. (b) $I-V$ curve for the pores in the opposite polarity, facing the bases (inset). (c) G vs spike number curves for the series arrangement with the pores in the same polarity. The sequences correspond to 2-ms positive and negative voltage pulses of amplitudes $V_p = 2$ V (blue curve) and 4 V (red curve). (d) G vs spike number curves for the pores in the opposite polarity.

Note also that the *capacitive current* associated with the changes of voltage V with time t leads to a shift in the nonzero crossing point of the $I-V$ curves [Figs. 2(a) and 2(b)]. This current can be estimated as $I_C(t) = CdV/dt = CV_0 2\pi f \cos(2\pi f t)$, where V_0 and f are the voltage amplitude and the frequency of the driving signal, and should be added to the conductive current to give the total current. The capacitance C can be estimated from the experimental membrane impedance $Z_{V\to 0}$ in the limits of voltage $V \to 0$ and high angular frequency f_{high} as $C2\pi f_{\text{high}} \simeq 1/Z_{V\to 0}$ [26]. For a multipore membrane with conical nanopores, we have measured $Z_{V\to 0} = 200\,\text{k}\Omega$ at $f_{\text{high}} = 2$ kHz [26]. Using the resulting estimation of C in Eq. (1), together with the typical values $f = 20s^{-1}$ and $V_0 = 2V$, the capacitive current is of the order of 0.1 μA at V = 2 V, in agreement with the experimental shift observed in the $I-V$ curves of Figs. 2(a) and 2(b). While this current is much lower than the conductive current, which is of the order of 10 μA, it can be noted experimentally because of the shift observed in the nonzero crossing point of the $I-V$ curves.

Figures 2(c) and 2(d) show the conductance (G) vs spike number curves of the membranes observed as responses to sequences of positive and negative voltage pulses (spikes) of duration 2 ms and amplitude $V_p = 1$ V (insets). The time lapse between two consecutive pulses is 2 ms. In these figures, each experimental point corresponds to the average conductance obtained for the pulse duration, excluding the initial capacitive peak [12]. The conductance responses of Figs. 2(c) and 2(d) are similar, as expected from their individual membrane characteristics [Figs. 2(a) and 2(b)]. Note also the neuromorphiclike responses [1–3] of the membrane to sequences of voltage pulses with different signs, suggesting gradual conductance increases and resets to the low conductance state.

Figures 3(a) and 3(b) show the $I-V$ curves obtained for the series arrangement, with the pores in the same and opposite (facing the bases) polarities, respectively. The series arrangements permit a broad range of electrical responses with different current rectifications and conductance regimes. Also, Fig. 3(a) shows the current that could be expected for the two membrane diodes of Figs. 2(a) and 2(b) arranged in series: the total resistance is approximately equal to the sum of the individual resistances, thus suggesting the validity of general voltage divider rules [19]. Also, the total voltage drop of 4 V in Fig. 3(a) is approximately divided into two individual drops of 2 V for each membrane because of their similar electrical characteristics [Figs. 2(a) and 2(b)]. As to Fig. 3(b), it shows no rectification because of the reversed pore polarity of sample 2 with respect to that of sample 1. Compare Fig. 3(a) with Fig. 3(b) for $V < 0$. In addition, Fig. 3(b) shows no pinched behavior and only one current loop because the current is now determined by the two low conductance (capacitive) branches of the individual (noncrossing) $I-V$ curves.

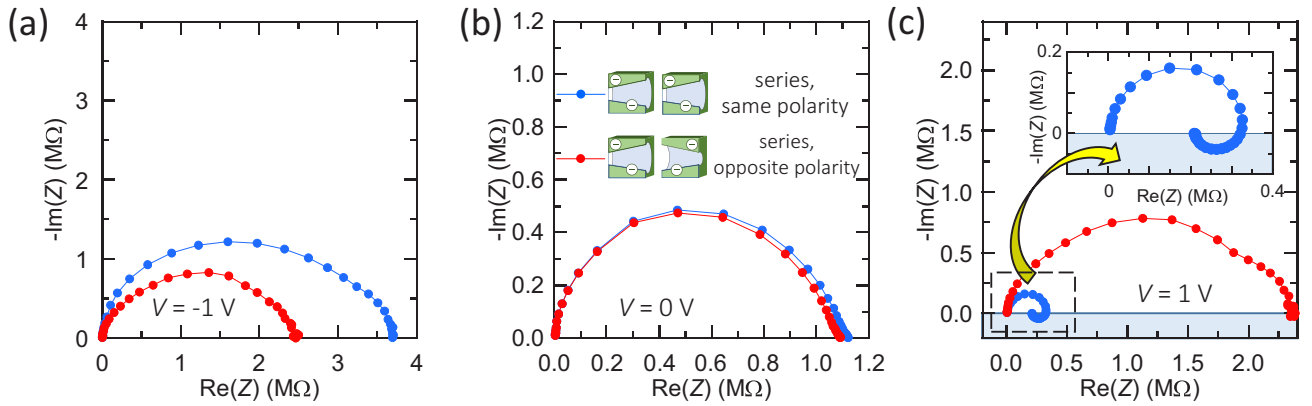

FIG. 4. (a) Imaginary $-\mathrm{Im}(Z)$ vs real $\mathrm{Re}(Z)$ (Nyquist) plots obtained for the series arrangements with the pores in the same (blue curve) and opposite (red curve) polarity in 0.1-M KCl solutions at a dc voltage $V = -1$ V. (b) Nyquist plots at a voltage amplitude of 0 V for the above series arrangements (insets). (c) Nyquist plots at $V = 1$ V. The blue highlighted region, which corresponds to the positive $\mathrm{Im}(Z)$ values, is zoomed for clarity (inset).

Figures 3(c) and 3(d) show the corresponding G vs spike number curves for the two series arrangements. In the case of Fig. 3(c), these curves are similar to those of the individual membranes [Figs. 2(c) and 2(d)] and show significant conductance potentiation for positive voltage pulses. In the case of opposite polarity [Fig. 3(d)], however, this potentiation is lost because of the decreased inductive response.

While reliable operation with individually different components could constitute an issue in the case of nanoscale pores and geometries [27] we have also checked that controlled arrangements of membranes with different individual characteristics may allow functionalities additional to those of Fig. 2. Note also that the different *on*/*off* conductance states and *inward*/*outward* rectifications of the $I-V$ curves shown in

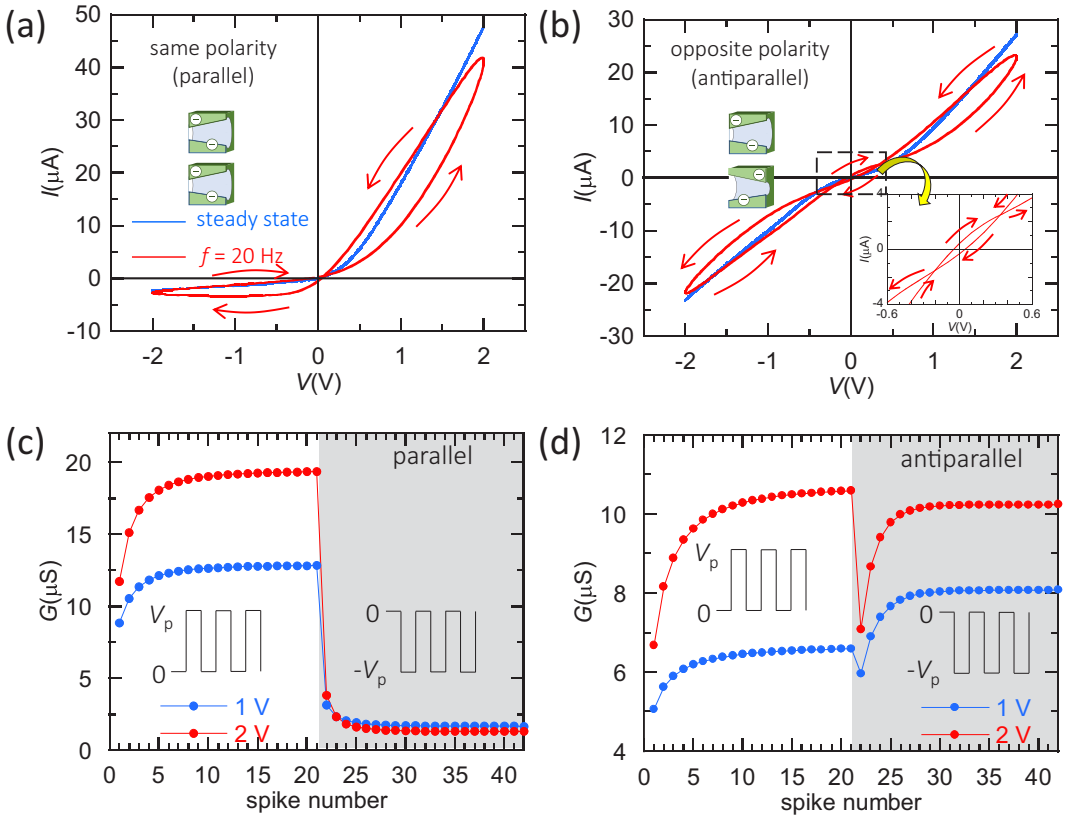

FIG. 5. (a) $I-V$ curve for samples 1 and 2 at $V_0 = 2$ V and $f = 20$ Hz in a 0.1-M KCl solution (red lines) for the parallel arrangement with the pores in the same polarity (inset). The steady-state curve (blue line) obtained at low signal frequency is also shown. (b) $I-V$ curve for the parallel arrangement with the pores in opposite polarity (antiparallel). The inset zooms the central loop. (c) G vs spike number curves for the parallel arrangement with the pores in the same polarity. The sequences correspond to 2-ms positive and negative voltage pulses of amplitudes $V_\mathrm{p} = 1$ V (blue curve) and $V_\mathrm{p} = 2$ V (red curve). (d) G vs spike number curves for the antiparallel arrangement.

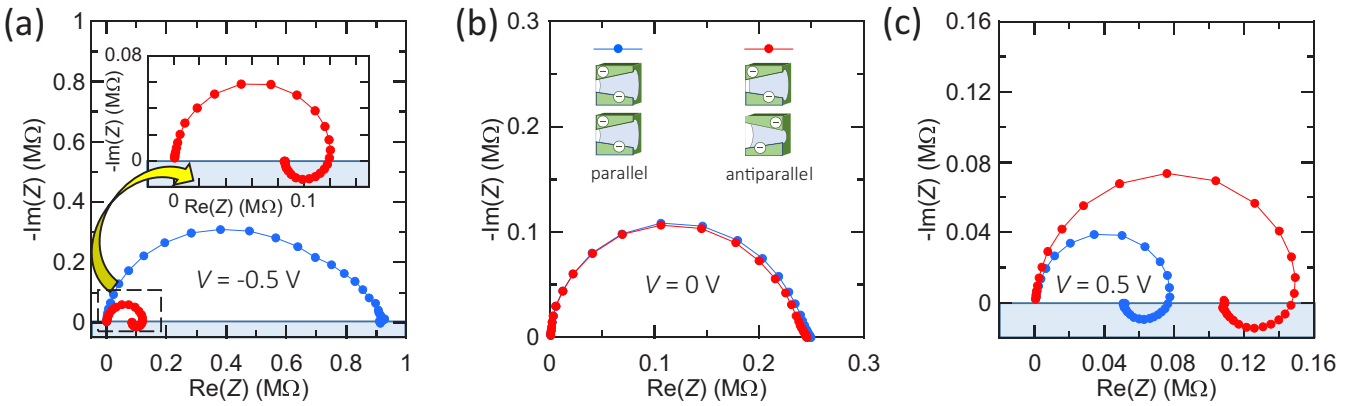

FIG. 6. (a) Nyquist plots obtained for the two parallel arrangements of Fig. 5 in 0.1-M KCl solutions at $V = -0.5$ V with the pores in the parallel (blue curve) and antiparallel (red curve and inset) arrangements. The blue highlighted region corresponds to positive Im(Z) values suggesting clear inductive effects. (b) Nyquist plots at $V = 0$ V. (c) Nyquist plots at $V = 0.5$ V.

Figs. 2 and 3 are reminiscent to those of the voltage-gated ion channels that regulate membrane potentials in the cell cycle and bioelectrochemical rhythms [17,28].

To characterize further the series arrangement, Figs. 4(a)–4(c) show the $-$Im(Z) vs Re(Z) (Nyquist) plots obtained with the membrane pores in the same and opposite polarities at different voltage amplitudes. As a control experiment, we have checked that the equivalent impedance of the series arrangement is approximately equal to the complex sum of the individual membrane impedances (results not shown). At negative voltages [Fig. 4(a)], similar impedances are obtained, with a dominant capacitive behavior, consistent with the absence of conductance potentiation that is observed in Figs. 3(c) and 3(d) at $V < 0$. This is also the case of a zero voltage [Fig. 4(b)]. Note however the region corresponding to positive Im(Z) values which is highlighted in Fig. 4(c) for positive voltages: there is a clear inductive behavior, and thus conductance potentiation [Fig. 3(c)] in the case of pores with the same polarity. On the contrary, there is a clear capacitive behavior, and thus absence of potentiation [Fig. 3(d)] in the case of pores with opposite polarity [Fig. 4(c)].

Figures 5(a)–5(d) correspond to the membrane samples connected in parallel. The case of the pores with the same polarity [parallel arrangement, Fig. 5(a)] gives a total current that is approximately the sum of the individual currents of Figs. 2(a) and 2(b), showing again the reliable response of the membrane arrangements. On the contrary, the arrangement with the pores in opposite polarity (antiparallel) shows an intriguing effect with a three-loop $I-V$ curve rather than the usual two-loop curve [Fig. 5(b)]. Note the two counterclockwise current loops observed at sufficiently high voltages together with the third clockwise central loop observed between -0.3 and $+0.3$ V [Fig. 5(b), inset]. The memory effect is reproducible and in agreement with the concavity changes observed in the steady state $I-V$ curve of Fig. 5(b). This case is opposite to that of Fig. 3(b): inductive loops can now exist at both $V > 0$ and $V < 0$ while a capacitive loop is observed around the origin, a reminiscent behavior to that observed in halide perovskite memristors [29].

The parallel arrangement of Fig. 5(c) shows a significant potentiation at positive voltage pulses but no potentiation at negative voltages. The steady values are approximately equal to the sum of the individual conductances of Figs. 2(c) and 2(d). In the case of the antiparallel arrangement, however, the $I-V$ curve of Fig. 5(b) shows conductive branches at $V > 0$ and $V < 0$, which gives conductance potentiation at both voltages as shown in Fig. 5(d) [30].

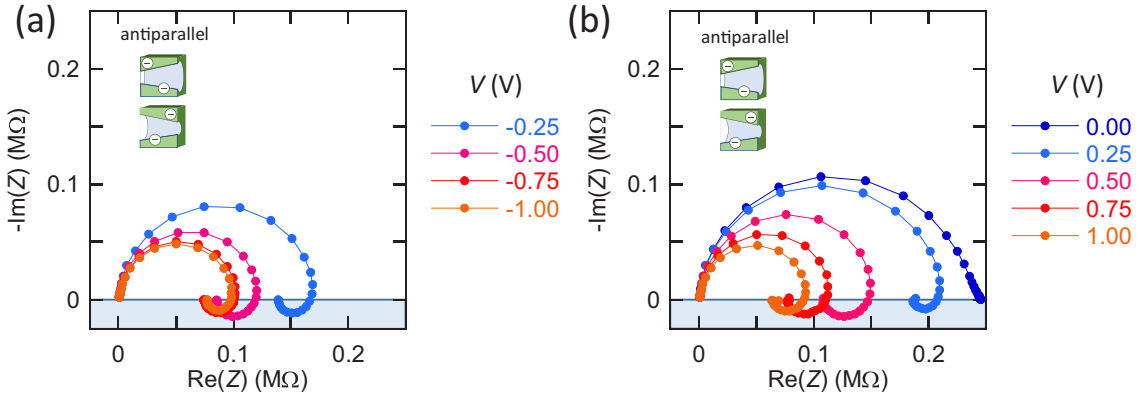

FIG. 7. (a) Nyquist plots for the antiparallel arrangement and 0.1-M KCl solutions at $V = -0.25$, -0.50, -0.75, and -1.00 V. (b) Nyquist plots for the antiparallel arrangement at $V = 0$, 0.25, 0.50, 0.75, and 1.00 V.

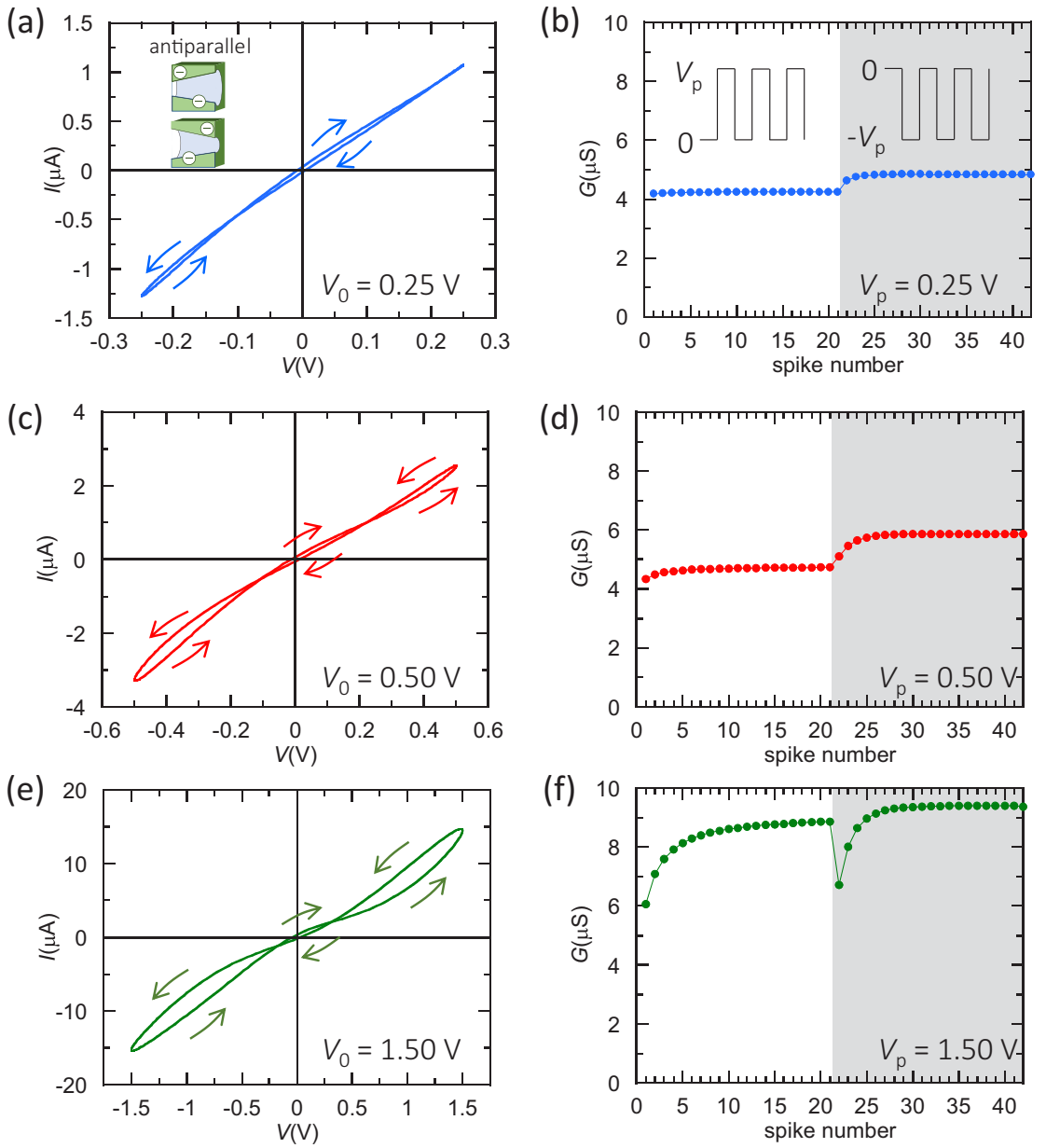

FIG. 8. (a) $I-V$ curve for the antiparallel arrangement in a 0.1-M KCl solution at $f = 20$ Hz and $V_0 = 0.25$ V. (b) The corresponding G vs spike number curves for two different voltage pulse sequences of 2 ms duration (insets) at $V_p = 0.25$ V. (c) $I-V$ curve at $V_0 = 0.50$ V. (d) G vs spike number curves at $V_p = 0.25$ V. (e) $I-V$ curve at $V_0 = 1.50$ V. (f) G vs spike number curves at $V_p = 1.25$ V. The grey region in the G vs spike number curves show the potentiation increase obtained when the voltage pulse approaches the inductive region of the $I-V$ curves.

Figures 6(a)–6(c) show the Im(Z) vs Re(Z) plots obtained for the two arrangements of Fig. 5 at different dc voltage values. Again, we have checked that the equivalent arrangement impedance can be written as $z_1 z_2/(z_1 + z_2)$, where z_1 and z_2 are the individual impedances of samples 1 and 2 in Fig. 2. At negative voltage [Fig. 6(a)], the parallel arrangement shows a purely capacitive behavior whose impedance is much higher than that obtained with the pores in the antiparallel arrangement, which shows a clear inductive behavior [Fig. 6(a), inset]. At zero voltage [Fig. 6(b)], the impedances of the two arrangements are equal and show a purely capacitive behavior. At positive voltage [Fig. 6(c)], the impedance of the pores in the parallel arrangement is lower than that of the pores in the antiparallel arrangement and both cases show an inductive behavior.

In order to investigate further the antiparallel arrangement, Figs. 7(a) and 7(b) shows the Nyquist plots for different negative and positive dc voltages. A clear inductive component can be observed over all the voltage range (blue highlighted region). At low absolute values of V this component is relatively small, in agreement with the central loop region of Fig. 5(b) showing no potentiation in Fig. 5(d). However, the inductive behavior increases with the absolute value of V until values higher than 0.5 V, where it decreases because of the enhanced Debye screening of the pore fixed charges caused by the increase of the ionic concentrations with V [13]. This fact

gives a concomitant decrease in the memory effects, which arise from the finite time electrical relaxation of the ions in the pore solution [12,13].

To better show the origin of the inductive effects, Figs. 8(a)–8(f) give the $I-V$ curves of the antiparallel arrangement, together with their corresponding G vs spike number curves, obtained parametrically in the voltage amplitude V_0. The curves show clearly the development of the capacitive component (central loop) with the voltage amplitude of the input signal. This experiment reveals that the width of this central loop hardly depends on V_0. Also, the G vs spike number curves clearly demonstrate the increase of the potentiation as the voltage pulse approaches the inductive region of the $I-V$ curves.

Summing up, Figs. 2(a) and 2(b), 3(a) and 3(b), 4(c), 5(a) and 5(b), 6(c), and 8(a), 8(c), and 8(e) associate the counterclockwise loops with the inductive behavior and the clockwise loops with the capacitive behavior [12]. Correspondingly, Figs. 2(c) and 2(d), 3(c) and 3(d), 5(c) and 5(d), and 8(b), 8(d), and 8(f) show conductance potentiation at $V > 0$ where the inductive behavior is significant. Thus, it is in order to provide now a theoretical explanation [12,13] for the chemical inductive effects observed. Note that the conical pore tips modulate the membrane ionic conduction due to its nanoscale dimensions. The high surface density of negative charges in this region gives a strongly nonlinear electric potential profile [13]. Thus, the mobile cations enter to the tip and accumulate at forward polarization $V > 0$ (high conductance) while they exit from the tip and are depleted for reverse polarization $V < 0$ (low conductance); see Figs. 2(a) and 2(b). Consequently, the significant inductive effects observed here arise from the high accumulation of mobile ions that has to be changed as the external driving signal changes with time, which leads to hysteresis and memory effects when the ionic solution at the pore tip cannot follow instantaneously the time changes of the signal [12].

IV. CONCLUSIONS

The memristive nanofluidic diodes presented here permit a broad range of ionic conduction properties that can be controlled not only by the amplitude and frequency of the external signal but also by simple membrane arrangements. The multipore membrane with conical nanopores allow significant current rectification because of the electrical interaction between the ionic solution and the pore surface charges. Memory and inductive effects are characterized by current-voltage curves, electrical impedance spectroscopy, and conductance potentiation by voltage pulses. These characteristics show physical insights that should be useful for the use of memristive arrangements in the design of electrochemical circuits where the modulation of conduction allows iontronics applications [31–40] including logic functions [32,33], memory [24,34,35], and associative learning [24,36,37].

ACKNOWLEDGMENTS

P.R., S.G., J.C., and S.M. acknowledge the support from the Conselleria d'Educació, Universitats i Ocupació (Generalitat Valenciana), Project No. CIAICO2022-247. J.B. acknowledges EUR2022-134045/AEI/1. We thank Dr. Saima Nasir and Dr. Mubarak Ali for preparing the membrane samples and Prof. Wolfgang Ensinger for his assistance.

[1] T. M. Kamsma, W. Q. Boon, T. ter Rele, C. Spitoni, and R. van Roij, Iontronic neuromorphic signaling with conical microfluidic memristors, Phys. Rev. Lett. **130**, 268401 (2023).

[2] B. Xie, T. Xiong, W. Li, T. Gao, J. Zong, Y. Liu, and P. Yu, Perspective on nanofluidic memristors: From mechanism to application, Chem. Asian J. **17**, e202200682 (2022).

[3] Y. Zhang, Z. Wang, Y. Yang J. Zhu, M. Rao, W. Song, Y. Zhuo, X. Zhang, M. Cui, L. Shen, R. Huang, and J. J. Yang, Brain-inspired computing with memristors: Challenges in devices, circuits, and systems, Appl. Phys. Rev. **7**, 011308 (2020).

[4] Z. S. Siwy, M. L. Bruening, and S. Howorka, Nanopores: Synergy from DNA sequencing to industrial filtration – small holes with big impact, Chem. Soc. Rev. **52**, 1983 (2023).

[5] Y. Hou, Y. Ling, Y. Wang, M. Wang, Y. Chen, X. Li, and X. Hou, Learning from the brain: Bioinspired nanofluidics, J. Phys. Chem. Lett. **14**, 2891 (2023).

[6] Q. Sheng, Y. Xie, J. Li, X. Wang, and J. Xue, Transporting an ionic-liquid/water mixture in a conical nanochannel: A nanofluidic memristor, Chem. Commun. **53**, 6125 (2017).

[7] P. Robin, T. Emmerich, A. Ismail, A. Niguès, Y. You, G.-H. Nam, A. Keerthi, A. Siria, A. K. Geim, B. Radha, and L. Bocquet, Long-term memory and synapse-like dynamics in two-dimensional nanofluidic channels, Science **379**, 161 (2023).

[8] A. Noy and S. B. Darling, Nanofluidic computing makes a splash, Science **379**, 143 (2023).

[9] T. Xiong, C. Li, X. He, B. Xie, J. Zong, Y. Jiang, W. Ma, F. Wu, J. Fei, P. Yu, and L. Mao, Neuromorphic functions with a polyelectrolyte-confined fluidic memristor, Science **379**, 156 (2023).

[10] Y. Hou and X. Hou, Bioinspired nanofluidic iontronics, Science **373**, 628 (2021).

[11] P. Zhang, M. Xia, F. Zhuge, Y. Zhou, Z. Wang, B. Dong, Y. Fu, K. Yang, Y. Li, Y. He, R. H. Scheicher, and X. S. Miao, Nanochannel-Based transport in an interfacial memristor can emulate the analog weight modulation of synapses, Nano Lett. **19**, 4279 (2019).

[12] P. Ramirez, V. Gomez, J. Cervera, S. Mafe, and J. Bisquert, Synaptical tunability of multipore nanofluidic memristors, J. Phys. Chem. Lett. **14**, 10930 (2023).

[13] J. Cervera, B. Schiedt, R. Neumann, S. Mafe, and P. Ramirez, Ionic conduction, rectification, and selectivity in single conical nanopores, J. Chem. Phys. **124**, 104706 (2006).

[14] I. Vlassiouk and Z. S. Siwy, Nanofluidic diode, Nano Lett. **7**, 552 (2007).

[15] P. Ramirez, V. Garcia-Morales, V. Gomez, M. Ali, S. Nasir, W. Ensinger, and S. Mafe, Hybrid circuits with nanofluidic diodes and load capacitors, Phys. Rev. Appl. **7**, 064035 (2017).

[16] J. S. Najem, G. J. Taylor, R. J. Weiss, M. S. Hasan, G. Rose, C. D. Schuman, A. Belianinov, C. P. Collier, and S. A. Sarles, Memristive ion channel-doped biomembranes as synaptic mimics, ACS Nano **12**, 4702 (2018).

[17] J. Cervera, M. Levin, and S. Mafe, Bioelectricity of non-excitable cells and multicellular pattern memories: Biophysical modeling, Phys. Rep. **1004**, 1 (2023).

[18] G. Perez-Mitta, A. G. Albesa, C. Trautmann, M. E. Toimil-Molares, and O. Azzaroni, Bioinspired integrated nanosystems based on solid-state nanopores: "iontronic" transduction of biological, chemical and physical stimuli, Chem. Sci. **8**, 890 (2017).

[19] M. Ali, P. Ramirez, S. Nasir, J. Cervera, S. Mafe, and W. Ensinger, Ionic circuitry with nanofluidic diodes, Soft Matter **15**, 9682 (2019).

[20] P. Apel, Track etching technique in membrane technology, Radiat. Meas. **34**, 559 (2001).

[21] Z. Siwy and A. Fulinski, Fabrication of a synthetic nanopore ion pump, Phys. Rev. Lett. **89**, 198103 (2002).

[22] T. Ma, J.-M. Janot, and S. Balme, Track-etched nanopore/membrane: From fundamental to applications, Small Methods **4**, 2000366 (2020).

[23] J. Bisquert, Inductive and capacitive hysteresis of current-voltage curves: Unified structural dynamics in solar energy devices, memristors, ionic transistors and bioelectronics, Phys. Rev. X Energy **3**, 011001 (2024).

[24] L. O. Chua and S. M. Kang, Memristive devices and systems, Proc. IEEE **64**, 209 (1976).

[25] Y. V. Pershin and M. Di Ventra, Memory effects in complex materials and nanoscale systems, Adv. Phys. **60**, 145 (2011).

[26] P. Ramirez, J. Cervera, S. Nasir, M. Ali, W. Ensinger, and S. Mafe, Electrochemical impedance spectroscopy of membranes with nanofluidic conical pores, J. Colloid Interface Sci. **655**, 876 (2024).

[27] J. Cervera, J. M. Claver, and S. Mafe, Individual variability and average reliability in parallel networks of heterogeneous biological and artificial nanostructures, IEEE Trans. Nanotechnol. **12**, 1198 (2013).

[28] J. R. M. Harvey, A. E. Plante, and A. L. Meredith, Ion channels controlling circadian rhythms in suprachiasmatic nucleus excitability, Physiol. Rev. **100**, 1435 (2020).

[29] L. Munoz-Diaz, A. J. Rosa, A. Bou, R. S. Sanchez, B. Romero, R. A. John, M. V. Kovalenko, A. Guerrero, and J. Bisquert, Inductive and capacitive hysteresis of halide perovskite solar cells and memristors under illumination, Front. Energy Res. **10**, 914115 (2022).

[30] J. Bisquert, Current-controlled memristors: Resistive switching systems with negative capacitance and inverted hysteresis, Phys. Rev. Appl. **20**, 044022 (2023).

[31] K. Xiao, L. Wen, and L. Jiang, Biomimetic solid-state nanochannels: From fundamental research to practical applications, Small **12**, 2810 (2016).

[32] I. Vourkas and G. C. Sirakoulis, Emerging memristor-based logic circuit design approaches: A review, IEEE Circuits Syst. Mag. **16**, 15 (2016).

[33] V. Gomez, P. Ramirez, J. Cervera, M. Ali, S. Nasir, W. Ensinger, and S. Mafe, Concatenated logic functions using nanofluidic diodes with all-electrical inputs and outputs, Electrochem. Commun. **88** 52 (2018).

[34] J. J. Perez-Grau, P. Ramirez, V. Garcia-Morales, J. Cervera, S. Nasir, M. Ali, W. Ensinger, and S. Mafe, Fluoride-induced negative differential resistance in nanopores: Experimental and theoretical characterization, ACS Appl. Mat. Int. **13**, 54447 (2021).

[35] P. Ramirez, J. Cervera, S. Nasir, M. Ali, W. Ensinger, and S. Mafe, Negative differential resistance and threshold-switching in conical nanopores with KF solutions, Appl. Phys. Lett. **118**, 181903 (2021).

[36] G. Dou, J. Liu, W. Guo, L. Liu, D. Zhang, and M. Guo, A liquid electrolyte-based memristor with application in associate learning, Appl. Phys. Lett. **123**, 124102 (2023).

[37] Q. Gao, J. Huang, J. Gao, X. Geng, Y. Ji, H. Li, G. Wang, B. Liang, M. Wang, Z. Xiao, Y. Zhu, P. K. Chu, and A. Huang, Tunable plasticity in functionalized honeycomb synaptic memristor for neurocomputing, Mater. Today Phys. **30**, 100947 (2023).

[38] D. Shi, W. Wang, Y. Liang, L. Duan, G. Du, and Y. Xie, Ultralow energy consumption angstrom-fluidic memristor, Nano Lett. **23**, 11662 (2023).

[39] X. Zhou, Y. Zong, Y. Wang, M. Sun, D. Shi, W. Wang, G. Du, and Y. Xie, Nanofluidic memristor based on the elastic deformation of nanopores with nanoparticle adsorption, Natl. Sci. Rev. **11**, nwad216 (2024).

[40] N. X. Armendarez, A. S. Mohamed, A. Dhungel, M. R. Hossain, M. S. Hasan, and J. S. Najem, Brain-inspired reservoir computing using memristors with tunable dynamics and short-term plasticity, ACS Appl. Mater. Interfaces **16**, 6176 (2024).